The manuscript is published in Applied Mathematical Modelling 2017, 45: 881–899
DOI: http://dx.doi.org/10.1016/j.apm.2017.01.042

A hybrid numerical model for multiphase fluid flow in a deformable porous medium

S. A. Ghoreishian Amiri[1,2*], S. A. Sadrnejad[2], H. Ghasemzadeh[2]

[1] Norwegian University of Science and Technology (NTNU), Trondheim, Norway
[2] Faculty of Civil Engineering, K.N. Toosi University of Technology, Tehran, Iran

Abstract

In this paper, a fully coupled finite volume-finite element model for a deforming porous medium interacting with the flow of two immiscible pore fluids is presented. The basic equations describing the system are derived based on the averaging theory. Applying the standard Galerkin finite element method to solve this system of partial differential equations does not conserve mass locally. A non-conservative method may cause some accuracy and stability problems. The control volume based finite element technique that satisfies local mass conservation of the flow equations can be an appropriate alternative. Full coupling of control volume based finite element and the standard finite element techniques to solve the multiphase flow and geomechanical equilibrium equations is the main goal of this paper. The accuracy and efficiency of the method are verified by studying several examples for which analytical or numerical solutions are available. The effect of mesh orientation is investigated by simulating a benchmark water-flooding problem. A representative example is also presented to demonstrate the capability of the model to simulate the behavior in heterogeneous porous media.

Keywords: Multiphase flow, Geomechanic, Hybrid solution, Fully coupled model

1. Introduction

Numerical simulation of multiphase fluid flows and mass transports in a deforming porous medium is of great interest in widely different fields of engineering. Areas of application include hydrocarbon

* Corresponding author
E-mail address: seyed.amiri@ntnu.no

reservoirs analysis [1], soil contamination problems [2], land subsidence due to ground fluids pumping [3] and consolidation analysis of partially saturated soils [4]. The governing equations of this system can be derived within the framework of averaging theory [5, 6] and consist of the conservation equations of mass and linear momentum in addition to appropriate constitutive and state equations.

Coupled multiphase hydro-mechanical problems have been modeled using a number of different numerical approaches which provide specific benefits for their intended fields of application (e.g. [3, 4, 7-19]). Sequential coupling of a multiphase flow finite difference (or finite volume) simulator with a finite element stress simulator is widely used in the field of reservoir engineering (e.g. [10, 12, 20]). Sequential coupling of different codes offers wide flexibility in software development perspective and can be less costly than a fully coupled scheme from the computational standpoint [15]. However, accuracy, stability and convergence properties of the solution can be affected by this kind of coupling [21]. In addition, since the physical discretization of two separate simulators can be different, a certain mapping of solutions might be required.

Full coupling of flow-deformation processes has the advantages of unconditional stability and internal consistency as the full system of the equilibrium and continuity equations are solved simultaneously. The Galerkin-type finite element method is usually employed for spatial discretization of the flow-deformation equations (e.g. [3, 4, 7-9, 11, 14, 21, 22]). Despite the advantages of this method in dealing with complex geometries and unstructured grids, it does not conserve mass locally and can produce some nonphysical oscillations.

Considering the different types of differential equations in coupled flow and deformation processes, i.e. elliptic displacement equation and parabolic pressure equation, hybrid methods of different numerical schemes can be employed to fulfill the requirements of each type of the equations. As already mentioned, there are several hybrid models in the literature proposed for sequential coupling, whereas a few hybrid approaches have been reported regarding the fully coupled methods.

To satisfy local mass conservation in the fully coupled solution of flow-deformation problems, some researchers proposed a hybrid solution with the mixed finite element discretization for flow and the Galerkin finite element method for deformation equations [16, 23-25]. The mixed finite element method is known to satisfy local conservation of mass and is able to deal with complex geometries and heterogeneities. The main difference of this method is that the velocity field is considered as a primary unknown variable rather than obtaining from the pressure solution. Although, the direct calculation of the velocity field provides more accurate description of the velocity solution, but increasing the number of primary unknowns results in a larger system of algebraic equations and thus, the computational cost could be the issue which may make the method inefficient.

In this paper, to reduce the number of primary unknowns in a fully coupled flow- deformation problem, the mixed finite element solution is proposed to be replaced by the control volume based finite element method. The control volume based finite element method is widely used in multiphase flow simulations (e.g. [26-33]). It combines the mesh flexibility of the finite element method with the local conservative characteristic of the finite volume scheme at the level of control volumes. The proposed method has the advantages of the mixed finite element solution in satisfying the mass conservation principle and in dealing with complex geometries and material discontinuities, but it is less costly from the computational standpoint, since the velocity filed is not included in the primary unknown variables. However, separate approximation of the pressure and velocity variables in the mixed finite element method, in general, provides more accurate flow results than the control volume based finite element method with the same number of elements.

The efficiency comparison between the mixed and control volume based finite element solution of the flow equations has been reported by Durlofsky [34]. Through several numerical examples, he showed that for systems with moderate degree of heterogeneity, the control volume based finite element method is the more computationally efficient alternative. It means that for a given number of unknown variables, it provides more accurate flow results. While, for higher degree of heterogeneity, for instance in sand/shale

systems, the mixed finite element method has been shown to predict more accurate results for flow equations than the control volume based finite element method with the same number of unknowns.

In this study, a hybrid solution with combining the control volume based finite element and the standard Galerkin finite element schemes is presented for full coupling of the multiphase flow and deformation equations. The capability of the flow solution for solving two-phase flow equations in highly heterogeneous porous media containing discontinuous material properties has been discussed in details in [32]. This method represents the discretized form of the equations at the level of elements, and consequently, similar to the classical finite element method, the complete system of algebraic equations can be obtained by assembling the element-wise equations. Effects of grid orientations and the application of the flow model for solving the black oil equations have been presented in [33].

2. Governing equations

The system of concern is a mixture of a deformable porous medium saturated with two (wetting and non-wetting) immiscible fluids. The system is described as the superposition of all phases, i.e. in the actual configuration, any spatial point $(\boldsymbol{x})$ in the domain spanned by the solid skeleton is simultaneously occupied by material points $(\boldsymbol{X}_\alpha)$ of all phases, while, the motion state of each phase is described independently.

Macroscopic state parameters and balance equations are obtained by integrating their microscopic counterparts based on the local averaging theory introduced by Hassanizadeh and Gray [5, 6]. In deriving the balance equations, the Lagrangian form is used for the solid skeleton, while motion of the fluid phases are described relative to the motion of the solid skeleton, i.e. the Eulerian form of the balance equations with respect to the motion of the solid skeleton are used for the fluid phases. Therefore, relative velocities of the fluids should be described referring to the motion of the solid skeleton:

$$\boldsymbol{w}_\alpha = \boldsymbol{v}_\alpha - \boldsymbol{v}_s, \quad \alpha \neq s \tag{1}$$

where $\boldsymbol{w}_\alpha$ is the relative velocity of phase α with respect to the solid skeleton, $\boldsymbol{v}_\alpha$ and $\boldsymbol{v}_s$ are the absolute velocities of phase α and solid skeleton, respectively. Moreover, the material time derivative of any differentiable function $f_\alpha(\boldsymbol{x},t)$, given in its spatial description, should be referred to the solid skeleton:

$$\frac{D^s f_\alpha}{Dt} = \frac{\partial f_\alpha}{\partial t} + (\nabla f_\alpha).\boldsymbol{v}_s \tag{2}$$

where $\frac{D^s(f_\alpha)}{Dt}$ indicates the material time derivative of function f (in phase α) with respect to the solid skeleton and ∇ denotes the vector gradient operator.

In the following, quasi static condition with irrotational velocity field in addition to small displacements and displacement gradients are assumed. So, the following expressions are considered:

$$\frac{\partial f}{\partial \boldsymbol{x}} \approx \frac{\partial f}{\partial \boldsymbol{X}} \tag{3}$$

$$\nabla^T \boldsymbol{v}_s = -\boldsymbol{m}^T \frac{D^s \boldsymbol{\varepsilon}}{Dt} \tag{4}$$

$$\boldsymbol{\varepsilon} = -\boldsymbol{L}\boldsymbol{u} \tag{5}$$

where f is an arbitrary differentiable function, $\boldsymbol{x}$ denotes the spatial coordinate, $\boldsymbol{X}$ stands for the material coordinate, $\boldsymbol{u}$ is the displacement vector of the solid skeleton, ∇^T indicates the divergence operator, and $\boldsymbol{\varepsilon}$, $\boldsymbol{L}$ and $\boldsymbol{m}^T$ are defined as:

$$\boldsymbol{\varepsilon} = \begin{bmatrix} \varepsilon_{xx} & \varepsilon_{yy} & \varepsilon_{zz} & \gamma_{xy} & \gamma_{yz} & \gamma_{zx} \end{bmatrix}^T \tag{6}$$

$$\boldsymbol{L} = \begin{bmatrix} \frac{\partial}{\partial x} & 0 & 0 & \frac{\partial}{\partial y} & 0 & \frac{\partial}{\partial z} \\ 0 & \frac{\partial}{\partial y} & 0 & \frac{\partial}{\partial x} & \frac{\partial}{\partial z} & 0 \\ 0 & 0 & \frac{\partial}{\partial z} & 0 & \frac{\partial}{\partial y} & \frac{\partial}{\partial x} \end{bmatrix}^T \tag{7}$$

$$\boldsymbol{m}^T = \begin{bmatrix} 1 & 1 & 1 & 0 & 0 & 0 \end{bmatrix} \tag{8}$$

where a superscript T refers to transpose. Note that throughout this paper, compressive stress and strain are assumed to be positive.

2.1. Mass balance equations

The mass balance equation for the solid phase can be written as:

$$\frac{D^s\left[(1-n)\rho_s\right]}{Dt}+(1-n)\rho_s\nabla^T\boldsymbol{v}_s=0 \tag{9}$$

where ρ_s is the solid phase density and n is the porosity of the medium. Substituting equation (4) into equation (9), variation of the porosity can be expressed by:

$$dn=-(1-n)\boldsymbol{m}^T d\boldsymbol{\varepsilon} \tag{10}$$

Similarly, the mass balance equations for wetting and non-wetting fluid phases can be written as:

$$\frac{D^s\left[n_\alpha\rho_\alpha\right]}{Dt}+\nabla^T(n_\alpha\rho_\alpha\boldsymbol{w}_\alpha)+n_\alpha\rho_\alpha\nabla^T\boldsymbol{v}_s=\dot{M}_\alpha,\quad \alpha\neq s \tag{11}$$

where n_α represents the volume fraction of phase α and $\dot{M}_\alpha$ is the source/sink term. The relative velocities of the fluids can be described with the generalized Darcy's law:

$$n_\alpha\boldsymbol{w}_\alpha=\frac{k_{r\alpha}\boldsymbol{K}}{\mu_\alpha}\left[\rho_\alpha\boldsymbol{g}-\nabla p_\alpha\right],\quad \alpha\neq s \tag{12}$$

where $\boldsymbol{g}$ is the acceleration vector due to gravity, p_α denotes the fluid pressure in phase α, $\boldsymbol{K}$ is the absolute permeability tensor, μ_α stands for the dynamic viscosity of phase α and $k_{r\alpha}$ is the relative permeability of phase α. The relative permeability of each phase can be expressed by [35]:

$$k_{rw}=\left(\frac{n_w-n_{wres}}{n_{wsat}-n_{wres}}\right)^{(2+3\lambda)/\lambda} \tag{13}$$

$$k_{rn}=\left(1-\frac{n_w-n_{wres}}{n_{wsat}-n_{wres}}\right)^2\left(1-\left[\frac{n_w-n_{wres}}{n_{wsat}-n_{wres}}\right]^{(2+\lambda)/\lambda}\right) \tag{14}$$

where n_{wsat} is the volume fraction of the wetting phase at zero suction, n_{wres} is the residual volume fraction of the wetting phase at very high suction, λ is a fitting parameter related to the pore size distribution and subscripts w and n refer to wetting and non-wetting phases, respectively.

Another equation can be derived by considering the fact that when two fluid phases flow in a porous medium, flow of each phase is affected by the other phase. The most practical method for considering this interacting motion is to use empirical correlations relating the capillary pressure ($p_c = p_n - p_w$) to the volume fraction of the wetting phase [36]. In this paper, the relation proposed by Brooks and Corey [37] is employed:

$$n_w = n_{wres} + \left(n_{wsat} - n_{wres}\right)\left[\frac{p_d}{p_c}\right]^{\lambda} \tag{15}$$

where p_d is the displacement pressure for the non-wetting phase and λ is the fitting parameter introduced in the relative permeability relations (Eqs. 13 & 14). In addition, It is assumed that the entire pore spaces are filled up with the fluids, i.e.

$$n = n_w + n_n \tag{16}$$

Differentiating (15) and (16) with considering (10), one can obtain:

$$dn_w = \frac{dn_w}{dp_c} dp_c = n'_w (dp_n - dp_w) \tag{17}$$

$$dn_n = -(1-n)\boldsymbol{m}^T d\boldsymbol{\varepsilon} - n'_w (dp_n - dp_w) \tag{18}$$

Substituting equations (4), (5), (12), (17) and (18) into equation (11), the final form of the flow equations are obtained:

$$\left[n_w \frac{d\rho_w}{dp_w} - \rho_w n'_w\right]\frac{D^s p_w}{Dt} + \rho_w n'_w \frac{D^s p_n}{Dt} + \nabla^T \left\{\rho_w \frac{k_{rw}\boldsymbol{K}}{\mu_w}\left[\rho_w \boldsymbol{g} - \nabla p_w\right]\right\} + \rho_w n_w \boldsymbol{m}^T \boldsymbol{L}\frac{D^s \boldsymbol{u}}{Dt} = \dot{M}_w \tag{19}$$

$$\left[n_n \frac{d\rho_n}{dp_n} - \rho_n n'_w\right]\frac{D^s p_n}{Dt} + \rho_n n'_w \frac{D^s p_w}{Dt} + \nabla^T \left\{\rho_n \frac{k_{rn}\boldsymbol{K}}{\mu_n}\left[\rho_n \boldsymbol{g} - \nabla p_n\right]\right\} + \rho_n (1-n+n_n) \boldsymbol{m}^T \boldsymbol{L}\frac{D^s \boldsymbol{u}}{Dt} = \dot{M}_n \tag{20}$$

The last term in the left-hand side of equations (19) and (20) shows the dependency of the flow pattern on the deformation of the solid skeleton.

2.2. Linear momentum balance equations

The linear momentum balance equation for the solid phase can be written as:

$$(1-n)\rho_s \frac{D^s \boldsymbol{v}_s}{Dt} + \boldsymbol{L}^T \left((1-n) \left(\boldsymbol{t}_s + \boldsymbol{m}^T \left(\frac{n_w}{n} p_w + \frac{n_n}{n} p_n \right) \right) \right) = \sum_{\alpha \neq s} \boldsymbol{T}_{s\alpha}^s + (1-n)\rho_s \boldsymbol{g} \tag{21}$$

where $\boldsymbol{t}_s$ is the inter-granular stress and $\boldsymbol{T}_{s\alpha}^s$ represents the rate of the linear momentum transferring to the solid phase due to its mechanical interaction with the motion of phase α. Similarly, the momentum balance equations for wetting and non-wetting fluid phases can be written as:

$$n_\alpha \rho_\alpha \frac{D^s \boldsymbol{v}_\alpha}{Dt} + \boldsymbol{L}^T (n_\alpha \boldsymbol{m} p_\alpha) + n_\alpha \rho_\alpha (\nabla \boldsymbol{v}_\alpha).\boldsymbol{w}_\alpha = \sum_{\beta \neq \alpha} \boldsymbol{T}_{\alpha\beta}^\alpha + n_\alpha \rho_\alpha \boldsymbol{g}, \qquad \begin{cases} \alpha = w, n \\ \beta = s, w, n \end{cases} \tag{22}$$

where $\boldsymbol{T}_{\alpha\beta}^\alpha$ represents the rate of the linear momentum transferring to phase α due to its mechanical interaction with phase β. The total linear momentum transferring from α to β is always equal to that from β to α, i.e.

$$\sum_\alpha \sum_{\beta \neq \alpha} \boldsymbol{T}_{\alpha\beta}^\alpha = 0., \qquad \alpha \& \beta = s, n, w \tag{23}$$

Considering equation (23), the momentum balance equation for the whole system can be obtained as the sum of equations (21) and (22):

$$\rho \frac{D^s \boldsymbol{v}_s}{Dt} + n_w \rho_w \frac{D^s \boldsymbol{w}_w}{Dt} + n_n \rho_n \frac{D^s \boldsymbol{w}_n}{Dt} + n_w \rho_w (\nabla \boldsymbol{v}_w).\boldsymbol{w}_w + n_n \rho_n (\nabla \boldsymbol{v}_n).\boldsymbol{w}_n + \boldsymbol{L}^T \boldsymbol{\sigma} = \rho \boldsymbol{g} \tag{24}$$

where ρ and $\boldsymbol{\sigma}$ are defined as [38]:

$$\rho = (1-n)\rho_s + \sum_{\alpha \neq s} n_\alpha \rho_\alpha \tag{25}$$

$$\boldsymbol{\sigma} = (1-n)\boldsymbol{t}_s + \sum_{\alpha \neq s} \frac{n_\alpha}{n} \boldsymbol{m} p_\alpha = \boldsymbol{\sigma}' + \frac{1}{n} \boldsymbol{m} (n_w p_w + n_n p_n) \tag{26}$$

where $\boldsymbol{\sigma}'$ is defined as the effective stress of the multiphase medium. It is assumed that the effective stress is responsible for all major deformations in the solid skeleton and can be linked to its strain by means of a constitutive relation:

$$d\boldsymbol{\sigma}' = \boldsymbol{D}_T d\boldsymbol{\varepsilon} \tag{27}$$

where $\boldsymbol{D}_T$ is considered as the tangential stiffness matrix.

Based on the assumptions of this study, acceleration terms of equation (24) and also the terms that depend on the gradient of the fluid velocity can be neglected. Time differentiating of the remains with considering equations (5), (10), (17), (18), (26) and (27), the final form of the linear momentum balance equation can be obtained:

$$\begin{aligned}&\boldsymbol{L}^T\left(-\boldsymbol{D}_T-\frac{1-n}{n^2}\boldsymbol{m}\left(n_w p_w-(n-n_n)p_n\right)\boldsymbol{m}^T\right)\boldsymbol{L}\frac{D^s\boldsymbol{u}}{dt}+\frac{1}{n}\boldsymbol{L}^T\boldsymbol{m}\left(n_w-n'_w p_w+n'_w p_n\right)\frac{D^s p_w}{Dt}\\&+\frac{1}{n}\boldsymbol{L}^T\boldsymbol{m}\left(n_n+n'_w p_w-n'_w p_n\right)\frac{D^s p_n}{Dt}=\dot{\rho}\boldsymbol{g}\end{aligned} \tag{28}$$

2.3. Initial and boundary conditions

Equations (19), (20) and (28) represent a system of highly nonlinear and strongly coupled partial differential equations defined on a domain Ω bounded by the boundary Γ. The fluid pressures (p_w & p_n) and skeleton deformations ($\boldsymbol{u}$) are selected as the primary unknown variables. In order to complete the system of equations, the initial and boundary conditions associated with the primary variables should be defined. The initial conditions should specify the full field of fluid phase pressures and skeleton deformations at time $t=0$:

$$\begin{cases}p_\alpha = p_\alpha^0, & \alpha \neq s\\ \boldsymbol{u}=\boldsymbol{u}^0\end{cases} \qquad \text{at } t=0. \quad \text{and} \quad \text{on } \Omega \ \& \ \Gamma \tag{29}$$

The Dirichlet boundary conditions are imposed as the prescribed values of the primary variables on the boundaries:

$$\begin{aligned} &p_\alpha = \overline{p}_\alpha, \quad \alpha \neq s \quad \text{on } \Gamma_{p_\alpha} \\ &\boldsymbol{u} = \overline{\boldsymbol{u}} \quad \text{on } \Gamma_u \end{aligned} \tag{30}$$

and the Neumann boundary conditions are imposed as the prescribed fluxes and tractions:

$$\begin{aligned} &\overline{\boldsymbol{q}}_\alpha = \left\{ \rho_\alpha \frac{k_{r\alpha}\boldsymbol{K}}{\mu_\alpha}\left(\rho_\alpha \boldsymbol{g} - \nabla p_\alpha\right) \right\}^T .\boldsymbol{n}, \quad \alpha \neq s \quad \text{on } \Gamma_{q_\alpha} \\ &\overline{\boldsymbol{t}} = \boldsymbol{l}^T \boldsymbol{\sigma} \quad \text{on } \Gamma_t \end{aligned} \tag{31}$$

where $\overline{\boldsymbol{q}}_w$ and $\overline{\boldsymbol{q}}_n$ are the imposed mass fluxes of wetting and non-wetting phases, respectively, $\overline{\boldsymbol{t}}$ is the imposed traction, $\boldsymbol{n}$ denotes the unit outward normal vector to the boundary:

$$\boldsymbol{n} = \begin{bmatrix} n_x & n_y & n_z \end{bmatrix}^T \tag{32}$$

and the matrix $\boldsymbol{l}$ is defined as:

$$\boldsymbol{l}^T = \begin{bmatrix} n_x & 0 & 0 & n_y & 0 & n_z \\ 0 & n_y & 0 & n_x & n_z & 0 \\ 0 & 0 & n_z & 0 & n_y & n_x \end{bmatrix} \tag{33}$$

The conditions of $\Gamma_u \bigcup \Gamma_t = \Gamma$, $\Gamma_{p_w} \bigcup \Gamma_{q_w} = \Gamma$ and $\Gamma_{p_n} \bigcup \Gamma_{q_n} = \Gamma$ should hold on the complementary parts of the boundary.

3. Numerical solution

As mentioned earlier, in this study, a control volume based finite element scheme is employed for spatial discretization of the fluid equations, while the standard Galerkin finite element method is used for the equilibrium equation. Hexahedral elements are employed for discretization of the physical domain and the numerical solution is implemented by expressing the primary unknown variables $(\boldsymbol{u}, p_w, p_n)$ in terms of their corresponding nodal values $(\boldsymbol{U}, \boldsymbol{p}_w, \boldsymbol{p}_n)$:

$$\boldsymbol{u} = \boldsymbol{N}\boldsymbol{U}, \quad p_w = \boldsymbol{N}\boldsymbol{p}_w, \quad p_n = \boldsymbol{N}\boldsymbol{p}_n \tag{34}$$

where $\boldsymbol{N}$ represents the standard finite element shape functions for hexahedral elements.

3.1. Fluid equations

In order to create the computational control volumes around the nodes of the finite element mesh, the centroids of the elements in the transformed space are joined to the midpoints of the corresponding sides (Fig. 1). Integrating equations (19) and (20) over a control volume, applying Gauss's theorem, using the interpolatory representation of the primary unknown variables (Eq. 34) and implementing the boundary conditions (Eq. 31), the weak form of the mass balance equations can be derived as:

$$\left[\int_{\Omega_{C.V.}}\left(n_w\frac{d\rho_w}{dp_w}-\rho_w n'_w\right)\boldsymbol{N}d\Omega\right]\frac{D^s\boldsymbol{p}_w}{Dt}+\left[\int_{\Omega_{C.V.}}\left(\rho_w n'_w\right)\boldsymbol{N}d\Omega\right]\frac{D^s\boldsymbol{p}_n}{Dt}-\left[\int_{\Gamma_{C.V.}-\Gamma_{q_w}}\left\{\rho_w\frac{k_{rw}\boldsymbol{K}}{\mu_w}\nabla\boldsymbol{N}\right\}^T.\boldsymbol{n}d\Gamma\right]^T\hat{\boldsymbol{p}}_w$$
$$+\left[\int_{\Omega_{C.V.}}\left(\rho_w n_w\right)\boldsymbol{m}^T\boldsymbol{B}d\Omega\right]\frac{D^s\boldsymbol{u}}{Dt}=\int_{\Omega_{C.V.}}\dot{M}_w d\Omega-\int_{\Gamma_{q_w}}\bar{q}_w d\Gamma-\int_{\Gamma_{C.V.}-\Gamma_{q_w}}\rho_w^2\left(\frac{k_{rw}\boldsymbol{K}}{\mu_w}\boldsymbol{g}\right)^T.\boldsymbol{n}d\Gamma \tag{35}$$

$$\left[\int_{\Omega_{C.V.}}\left(n_n\frac{d\rho_n}{dp_n}-\rho_n n'_w\right)\boldsymbol{N}d\Omega\right]\frac{D^s\boldsymbol{p}_n}{Dt}+\left[\int_{\Omega_{C.V.}}\left(\rho_n n'_w\right)\boldsymbol{N}d\Omega\right]\frac{D^s\boldsymbol{p}_w}{Dt}-\left[\int_{\Gamma_{C.V.}-\Gamma_{q_n}}\left\{\rho_n\frac{k_{rn}\boldsymbol{K}}{\mu_n}\nabla\boldsymbol{N}\right\}^T.\boldsymbol{n}d\Gamma\right]^T\hat{\boldsymbol{p}}_n$$
$$+\left[\int_{\Omega_{C.V.}}\left(\rho_n(1-n)+\rho_n n_n\right)\boldsymbol{m}^T\boldsymbol{B}d\Omega\right]\frac{D^s\boldsymbol{u}}{Dt}=\int_{\Omega_{C.V.}}\dot{M}_n d\Omega-\int_{\Gamma_{q_n}}\bar{q}_n d\Gamma-\int_{\Gamma_{C.V.}-\Gamma_{q_n}}\rho_n^2\left(\frac{k_{rn}\boldsymbol{K}}{\mu_n}\boldsymbol{g}\right)^T.\boldsymbol{n}d\Gamma \tag{36}$$

where $\Omega_{C.V.}$ indicates the domain of a control volume bounded by $\Gamma_{C.V.}$, and $\boldsymbol{B}(=\boldsymbol{LN})$ is the strain-displacement matrix.

Equations (35) and (36) present the discretized form of the mass balance equations at the level of control volumes. In order to represent the equations at the level of elements, each control volume around a node should be divided to number of sub-control volumes, each sub-control volume belongs to a specific element associated with the node (Fig. 2). Similarly, each face of a control volume should also be divided to sub-control volume faces. Integration over a control volume or a control volume face can be calculated by summing up the individual integrations over the associated sub-control volumes or sub-control volume faces, accordingly. Hence, discretized form of the equations are represented at the level of elements and the complete form of the balance equations can be obtained by assembling the element-wise formulation similar to the classical finite element method. The element-wise representation of equations (35) and (36) are

$$\bar{\boldsymbol{P}}_{ww}\boldsymbol{p}_w + \boldsymbol{P}_{ww}\frac{D^s\boldsymbol{p}_w}{Dt} + \boldsymbol{C}_{wn}\frac{D^s\boldsymbol{p}_n}{Dt} + \boldsymbol{C}_{wn}\frac{D^s\boldsymbol{U}}{Dt} = \boldsymbol{f}_w \tag{37}$$

$$\bar{\boldsymbol{P}}_{nn}\boldsymbol{p}_n + \boldsymbol{C}_{nw}\frac{D^s\boldsymbol{p}_w}{Dt} + \boldsymbol{P}_{nn}\frac{D^s\boldsymbol{p}_n}{Dt} + \boldsymbol{C}_{nu}\frac{D^s\boldsymbol{U}}{Dt} = \boldsymbol{f}_n \tag{38}$$

where the coefficients are described as:

$$\bar{\boldsymbol{P}}_{ww} = -\int_{\Gamma_{\text{S.C.V.}}-\Gamma_{q_w}} \boldsymbol{W}^T \left\{ \left(\rho_w \frac{k_{rw}\boldsymbol{K}}{\mu_w} \nabla \boldsymbol{N} \right)^T . \boldsymbol{n} \right\}^T d\Gamma \tag{39}$$

$$\bar{\boldsymbol{P}}_{nn} = -\int_{\Gamma_{\text{S.C.V.}}-\Gamma_{q_n}} \boldsymbol{W}^T \left\{ \left(\rho_n \frac{k_{rn}\boldsymbol{K}}{\mu_n} \nabla \boldsymbol{N} \right)^T . \boldsymbol{n} \right\}^T d\Gamma \tag{40}$$

$$\boldsymbol{P}_{ww} = \int_{\Omega_e} \boldsymbol{W}^T \left(n_w \frac{d\rho_w}{dp_w} - \rho_w n'_w \right) \boldsymbol{N} d\Omega \tag{41}$$

$$\boldsymbol{P}_{nn} = \int_{\Omega_e} \boldsymbol{W}^T \left(n_n \frac{d\rho_n}{dp_n} - \rho_n n'_w \right) \boldsymbol{N} d\Omega \tag{42}$$

$$\boldsymbol{C}_{wn} = \int_{\Omega_e} \boldsymbol{W}^T \left(\rho_w n'_w \right) \boldsymbol{N} d\Omega \tag{43}$$

$$\boldsymbol{C}_{nw} = \int_{\Omega_e} \boldsymbol{W}^T \left(\rho_n n'_w \right) \boldsymbol{N} d\Omega \tag{44}$$

$$\boldsymbol{C}_{wu} = \int_{\Omega_e} \boldsymbol{W}^T \left(\rho_w n_w \right) \boldsymbol{m}^T \boldsymbol{B} d\Omega \tag{45}$$

$$\boldsymbol{C}_{nu} = \int_{\Omega_e} \boldsymbol{W}^T \left(\rho_n (1-n) + \rho_n n_n \right) \boldsymbol{m}^T \boldsymbol{B} d\Omega \tag{46}$$

$$\boldsymbol{f}_w = \int_{\Omega_e} \dot{M}_w \boldsymbol{W}^T d\Omega - \int_{\Gamma_{q_w}} \bar{q}_w \boldsymbol{W}^T d\Gamma - \int_{\Gamma_{\text{S.C.V.}}-\Gamma_{q_w}} \left[\rho_w^2 \left(\frac{k_{rw}\boldsymbol{K}}{\mu_w} \boldsymbol{g} \right)^T . \boldsymbol{n} \right] \boldsymbol{W}^T d\Gamma \tag{47}$$

$$\boldsymbol{f}_n = \int_{\Omega_e} \dot{M}_n \boldsymbol{W}^T d\Omega - \int_{\Gamma_{q_n}} \bar{q}_o \boldsymbol{W}^T d\Gamma - \int_{\Gamma_{\text{S.C.V.}}-\Gamma_{q_n}} \left[\rho_n^2 \left(\frac{k_{rn}\boldsymbol{K}}{\mu_n} \boldsymbol{g} \right)^T . \boldsymbol{n} \right] \boldsymbol{W}^T d\Gamma \tag{48}$$

where Ω_e and $\Gamma_{\text{S.C.V.}}$ indicate the domain of the elements and the boundaries of the sub-control volumes, respectively, and $\boldsymbol{W}$ is the vector of weighting functions. The weighting functions in this method are

chosen such that the *i*th weighting function of an element takes a constant value of unity over the sub-control volume associated with node *i* and zero elsewhere in the element (Fig. 3), i.e.

$$W_i = \begin{cases} 1 & \text{in the sub-control volume belongs to node i} \\ 0 & \text{elsewhere} \end{cases} \tag{49}$$

Hence, the equations are presented at the level of elements, while calculations are actually performed at the control volume level. Consequently, discontinuity of the velocity field between adjacent elements does not affect the local conservative characteristic of the calculations over the control volumes (Fig. 4).

3.2. Equilibrium equations

Applying the standard Galerkin finite element discretization technique to equation (28) along with the boundary condition (Eq. 31), the discretized form of the equilibrium equation can be derived in the form of:

$$\boldsymbol{C}_{uw}\frac{D^s \boldsymbol{p}_w}{Dt} + \boldsymbol{C}_{un}\frac{D^s \boldsymbol{p}_n}{Dt} + \boldsymbol{K}_{uu}\frac{D^s \boldsymbol{U}}{Dt} = \boldsymbol{f}_u \tag{50}$$

where the coefficient are described as:

$$\boldsymbol{C}_{uw} = \int_{\Omega_e} \boldsymbol{B}^T \frac{1}{n}\boldsymbol{m}\left(n_w - n'_w p_w + n'_w p_n\right)\boldsymbol{N}d\Omega \tag{51}$$

$$\boldsymbol{C}_{un} = \int_{\Omega_e} \boldsymbol{B}^T \frac{1}{n}\boldsymbol{m}\left(n_n + n'_w p_w - n'_w p_n\right)\boldsymbol{N}d\Omega \tag{52}$$

$$\boldsymbol{K}_{uu} = \int_{\Omega_e} \boldsymbol{B}^T \left(-\boldsymbol{D}_T - \frac{(1-n)}{n^2}\boldsymbol{m}\left[n_w p_w - (n-n_n)p_n\right]\boldsymbol{m}^T\right)\boldsymbol{B}d\Omega \tag{53}$$

$$\boldsymbol{f}_u = -\int_{\Omega_e} \boldsymbol{N}^T \dot{\rho}\boldsymbol{g}d\Omega + \int_{\Gamma_t} \boldsymbol{N}^T \bar{\boldsymbol{t}}d\Gamma \tag{54}$$

The Gaussian quadrature approach is employed for calculating the integrals in coefficients (39)-(48) and (51)-(54).

3.3. Time discretization

Since spatial discretization has been carried out, equations (37), (38) and (50) represent a set of ordinary differential equations in time:

$$\begin{bmatrix} \bar{\boldsymbol{P}}_{ww} & 0 & 0 \\ 0 & \bar{\boldsymbol{P}}_{nn} & 0 \\ 0 & 0 & 0 \end{bmatrix} \begin{bmatrix} \boldsymbol{p}_w \\ \boldsymbol{p}_n \\ \boldsymbol{U} \end{bmatrix} + \begin{bmatrix} \boldsymbol{P}_{ww} & \boldsymbol{C}_{wn} & \boldsymbol{C}_{wu} \\ \boldsymbol{C}_{nw} & \boldsymbol{P}_{nn} & \boldsymbol{C}_{wn} \\ \boldsymbol{C}_{uw} & \boldsymbol{C}_{un} & \boldsymbol{K}_{uu} \end{bmatrix} \frac{D^s}{Dt} \begin{bmatrix} \boldsymbol{p}_w \\ \boldsymbol{p}_n \\ \boldsymbol{U} \end{bmatrix} = \begin{bmatrix} \boldsymbol{f}_w \\ \boldsymbol{f}_n \\ \boldsymbol{f}_u \end{bmatrix} \tag{55}$$

The time discretization of the equations is performed by the fully implicit first order accurate finite difference scheme

$$\begin{bmatrix} \boldsymbol{P}_{ww} + \Delta t \bar{\boldsymbol{P}}_{ww} & \boldsymbol{C}_{wn} & \boldsymbol{C}_{wu} \\ \boldsymbol{C}_{nw} & \boldsymbol{P}_{nn} + \Delta t \bar{\boldsymbol{P}}_{nn} & \boldsymbol{C}_{wn} \\ \boldsymbol{C}_{uw} & \boldsymbol{C}_{un} & \boldsymbol{K}_{uu} \end{bmatrix}_{n+1} \begin{bmatrix} \Delta \boldsymbol{p}_w \\ \Delta \boldsymbol{p}_n \\ \Delta \boldsymbol{U} \end{bmatrix}_{n+1} = \Delta t \begin{bmatrix} \boldsymbol{f}_w \\ \boldsymbol{f}_n \\ \boldsymbol{f}_u \end{bmatrix}_{n+1} - \Delta t \begin{bmatrix} \bar{\boldsymbol{P}}_{ww} & 0 & 0 \\ 0 & \bar{\boldsymbol{P}}_{nn} & 0 \\ 0 & 0 & 0 \end{bmatrix}_{n+1} \begin{bmatrix} \boldsymbol{p}_w \\ \boldsymbol{p}_n \\ \boldsymbol{U} \end{bmatrix}_n \tag{56}$$

where $\Delta t (= t_{n+1} - t_n)$ is the time step increment and $\Delta(*)_{n+1} = (*)_{n+1} - (*)_n$.

Equation (56) represents a system of highly nonlinear algebraic equations which is solved using the Global Inexact Affine Invariant Newton Technique (GIANT) [39]. This requires calculating the residual and requiring it to vanish. To continue, equation (56) and its residual form are rewritten in the following simple format

$$\left(\boldsymbol{A} + \Delta t \boldsymbol{Q}\right)_{n+1} \Delta \boldsymbol{X}_{n+1} = \left(\Delta t \boldsymbol{F}\right)_{n+1} - \left(\Delta t \boldsymbol{Q}\right)_{n+1} \boldsymbol{X}_n \tag{57}$$

$$\boldsymbol{R}\left(\Delta \boldsymbol{X}_{n+1}\right) = \left(\boldsymbol{A} + \Delta t \boldsymbol{Q}\right)_{n+1} \Delta \boldsymbol{X}_{n+1} - \left(\Delta t \boldsymbol{F}\right)_{n+1} + \left(\Delta t \boldsymbol{Q}\right)_{n+1} \boldsymbol{X}_n = 0 \tag{58}$$

Linearizing the residual using Taylor series expansion about $\Delta \boldsymbol{X}$ and neglecting higher-order terms gives

$$\boldsymbol{R}\left(\Delta \boldsymbol{X}_{n+1}\right) = \boldsymbol{R}\left(\Delta \boldsymbol{X}^i_{n+1}\right) + \left.\frac{\partial \boldsymbol{R}}{\partial\left(\Delta \boldsymbol{X}\right)}\right|_{\Delta \boldsymbol{X}^i_{n+1}} \left(\Delta \boldsymbol{X}^{i+1}_{n+1} - \Delta \boldsymbol{X}^i_{n+1}\right) \tag{59}$$

where $\left.\frac{\partial \boldsymbol{R}}{\partial\left(\Delta \boldsymbol{X}\right)}\right|_{\Delta \boldsymbol{X}^i_{n+1}} = \boldsymbol{J}$ is called the Jacobian matrix. To complete the description of the solution, it is necessary to evaluate the Jacobian matrix. The complete form of the Jacobian is expressed as

$$\boldsymbol{J} = \left(\boldsymbol{A} + \Delta t \boldsymbol{Q}\right)_{n+1}^{i} + \left.\frac{\partial \boldsymbol{A}}{\partial \Delta \boldsymbol{X}}\right|_{\Delta \boldsymbol{X}_{n+1}^{i}} \Delta \boldsymbol{X}_{n+1}^{i} + \Delta t \left.\frac{\partial \boldsymbol{Q}}{\partial \Delta \boldsymbol{X}}\right|_{\Delta \boldsymbol{X}_{n+1}^{i}} \Delta \boldsymbol{X}_{n+1}^{i} \tag{60}$$

However, due to classification and discussion made by Settari and Aziz [40], the following approximation of the Jacobian is generally enough for solving the system of the equations

$$\boldsymbol{J} \approx \left(\boldsymbol{A} + \Delta t \boldsymbol{Q}\right)_{n+1}^{i} + \Delta t \left.\frac{\partial \boldsymbol{Q}}{\partial \Delta \boldsymbol{X}}\right|_{\Delta \boldsymbol{X}_{n+1}^{i}} \Delta \boldsymbol{X}_{n+1}^{i} \tag{61}$$

Finally, it should be noted that the system of linearized equation may become ill-conditioned as the diagonal terms in $\boldsymbol{K}_{uu}$ can be many orders of magnitude greater than the terms in $\bar{\boldsymbol{P}}_{ww}$ and $\bar{\boldsymbol{P}}_{nn}$. Indeed, in case of very steep slope of the capillary curve, very small terms may appear in $\boldsymbol{C}_{wn}$ and $\boldsymbol{C}_{nw}$. To avoid ill-conditioning it is possible to scale the various terms in equation (56). This approach is suggested by Reed [41] and successfully used in Lewis and Schrefler [42] and Sloan and Abbo [43].

4. Numerical examples

In this section, the proposed model is verified by resolution of three 1D problems for which analytical or numerical solutions are available. Firstly, the flow side of the model is verified using the 1D Van Duijn and De Neef problem [44]. The coupled solution is then validated against consolidation problems of a soil column saturated with one and two immiscible fluids. The effect of mesh orientation is then investigated using a benchmark water-flooding problem. Finally, the solution of a five spot water-flooding problem in a highly heterogeneous deformable porous medium is presented as the last example.

4.1. Van Duijn-De Neef problem

Countercurrent flow of two immiscible fluids in a 1D horizontal domain of length 200 m is considered. The domain is composed of two rigid porous media with equal lengths. Impermeable boundary condition is applied at the both ends of the domain. The left-hand side (part 1) and the right-hand side (part 2) of the domain are initially saturated with the wetting and non-wetting fluids, respectively. Due to the contrast in capillary pressure at the interface, redistribution of the fluids is expected. In this example, two cases with

different permeability and capillary pressure distribution are considered. In the first case, same properties for the two parts of the domain are assumed, whereas in the second case, more permeable medium with lower capillary pressure is used for part 1. The material properties and model parameters for both cases are listed in table 1. Van Duijn and De Neef [44] provide a semi-analytical solution for this problem. The numerical and semi-analytical solutions at different times are compared in figure 5, and reasonable agreements are achieved. However, since water saturation is calculated on the integration points of the associated sub-control volumes and then it is mapped to the nodes, and due to the difference of water saturation on the sides of the interface of parts 1 and 2, an averaged value of water saturation is obtained at the interface (point a in figure 5).

The problem is also solved in [45] using a hybrid mixed finite element-discontinuous Galerkin scheme. Figure 6 represents their results for case 2. Comparing figures 5 and 6, it can be seen that the mixed finite element scheme provides more accurate results by using the same number of elements, i.e. 100 elements. However, using a more refined mesh of 200 elements for the proposed model, both methods produce almost same accuracy (figure 7).

4.2. One dimensional-one phase consolidation problem

This problem consists of a porous column bounded by rigid and impermeable walls, except on its top, where it is loaded by a pressure p, and free to drain. Initially, the pore pressure in the domain is zero, but upon loading, it jumps to the maximum value. Immediately after loading, the fluid in the domain should begin to drain through the drainage boundary. The relevant data for this simulation is illustrated in figure 8. Analytical solution of this problem can be found in [46]. Figure 9 shows the comparison of the analytical and numerical solutions at different times, and well agreement is achieved.

To investigate the convergence of the proposed model, a non-dimensional time scale (t^*) is introduced and the problem is solved with different meshes and time step sizes

$$t^* = \frac{(1-\upsilon)E}{(1+\upsilon)(1-2\upsilon)} k\, t / \left(\mu H^2\right) \tag{62}$$

where E and υ are the elastic modulus and Poisson's ratio of the soil matrix and H is the length of the system. The problem is solved with fixed $\Delta t^* = 3.6E-5$ and uniform meshes of 5, 10, 20 and 40 elements. In addition, to check the Δt-convergence, the problem is also solved with a fixed uniform mesh of 20 elements and time steps equal to $\Delta t^* = 3.6E-3$, $1.8E-3$, $7.2E-4$ and $3.6E-4$. Figure 10 shows the results of the convergence study.

It should be noted that the spatial stability of fully coupled solutions in the very initial stages of consolidation problems, or generally whenever almost undrained conditions are encountered, is always an issue. The required stability condition for this kind of problems has been investigated by Vermeer and Verruijt [47], which required the time steps to be larger than a certain value, otherwise oscillation will occur. Upon further study, Wan [48] showed that the mechanism behind this oscillation is what is generally called the saddle point problem, where the solution is a stationary value. To change the saddle point nature of the equations to a parabolic problem, he proposed to add two stabilizing terms to the coefficient matrix. In this study, the stability condition proposed by Vermeer and Verruijt [47] is followed for determining the time steps of the simulations.

4.3. One dimensional-two phase consolidation problem

In order to examine the coupled behavior of the model at the presence of two phase fluid flow, a poro-elastic soil column problem, presented by Li et al. [7], is considered. The soil column is saturated with two immiscible fluids and subjected to a step loading with a ramp between $t = 0$ and $t = 1$ second (Fig. 11). The boundary conditions and the material properties of this simulation are also shown. Figure 12 illustrates the distribution of pressure and vertical effective stress at different times. It shows that the results of the present model is in a reasonable agreement with those presented in [7].

4.4. Radial flow

The problem analyzed in this section was originally proposed by Bajor and Cormack [49], and modified by Hurtado et al. [50] to evaluate the grid orientation effects in multiphase flow simulations, but it could be also appropriate to check the effect in a coupled geomechanics-multiphase flow simulator. The problem is schematically depicted in figure 13. The domain is initially oil saturated, and its initial pressure is equal to zero. The total pressure at the outflow boundaries is also equal to zero, so the following system of equations should be considered:

$$p = \frac{n_w}{n} p_w + (1 - \frac{n_w}{n}) p_o = 0. \tag{63}$$

$$p_c = p_o - p_w \tag{64}$$

These equations are iteratively coupled with the whole system to ensure the fulfillment of the above-mentioned restrictions at the outflow boundaries. For the mechanical boundary conditions, it is assumed that displacements at the lower boundary of the domain are fixed to zero, while for the vertical boundaries, lateral displacements are fixed. The other relevant data of the simulation are listed in table 2.

For a more sever example to investigating the grid orientation effects, the following relations are considered for the relative permeability functions [51]:

$$k_{rw} = \frac{s_e^N}{M(1 - s_e^N) + s_e^N} \quad , \begin{cases} N = 2 & \text{case 1} \\ N = 3 & \text{case 2} \end{cases} \tag{65}$$

$$k_{ro} = 1 - k_{rw} \tag{66}$$

where

$$s_e = \frac{n_w - n_{wres}}{n_{wsat} - n_{wres}} \tag{67}$$

$$M = \frac{\mu_o}{\mu_w} \tag{68}$$

The problem is solved with two 20×20 regular and randomly distorted grids for both cases ($N = 2$ and $N = 3$). For the first case (i.e. $N = 2$), the resultant water saturation fields after 0.2 PV (pore volume) of water injection are shown in figure 14. As shown in the figure, the results from the two meshes fitted reasonably well, with the predicted circle shapes for the water front showing minimal grid orientation effects. The water saturation contours for the second case (i.e. $N = 3$) are illustrated in figure15. As shown in the figure, the shape of the water front deviated from the expected circle shape. Even with this instability of the water front, further investigation of the results for the water breakthrough time (figure 16) shows that the results from the two meshes are in reasonable agreement with each other.

4.5. Five spot water-flooding problem in a deformable continuous heterogeneous porous medium

A quarter of a five-spot water-flooding problem in a deformable porous medium is considered in this example. The absolute permeability of the medium is defined by [52]:

$$\log_{10}^{K} = -7 + \sin(10\pi\bar{x})\sin(10\pi\bar{y}) + 0.7\sin(3\pi\bar{x})\cos(6\pi\bar{y}) + 0.3\sin(0.5\pi\bar{x})\sin(\pi\bar{y}) \tag{69}$$

where $\bar{x} = x/300$ and $\bar{y} = y/300$. The physical domain, computational mesh and absolute permeability distribution are illustrated in figure 17. The initial and the mechanical boundary conditions of the reservoir are considered the same as those presented in section 4.4. Water is injected into the domain from the left well and with the rate of 300 ton/day. Equations (63) and (64) are considered as the boundary conditions of the production well. The other relevant data of the simulation are listed in tables 3 and 4. Figure 18 shows the contour plot of water saturation distribution and the streamlines after 100 days of injection. Due to the geomechanical coupling, variation of pore pressure results in deformation of the reservoir rock. At the same time, reservoir deformation affect the pattern of pressure and consequently the efficiency of the production plan. Figure 19 illustrates the x-direction and y-direction displacement distribution after 100 days of injection.

5. Conclusions

In the present paper, a hybrid numerical model was presented to simulate the coupling of geomechanincs and two immiscible fluids flow under isothermal conditions. The conservation equations of mass and linear momentum together with hydraulic and mechanical constitutive relations for the pore fluids and solid skeleton constituted the basis of the multiphase formulation. A fully coupled hybrid spatial discretization by means of control volume based finite element method for fluid equations, and Galerkin finite element method for equilibrium equations was performed. The fully implicit first order accurate finite difference scheme was employed for time discretization of the equations. The method preserves local conservation of mass and is capable of handling complex geometries and heterogeneities. In order to exemplify that the model is efficient and effective in simulating multiphase fluids flow in deformable porous media, it was successfully applied to several numerical examples. Three benchmark problems were chosen to illustrate the accuracy of the computational algorithm. Two representative examples were also presented in order to investigate the so-called mesh orientation effect and also to illustrate the capability of the model to simulate the behavior in heterogeneous porous media.

References

[1] M.D. Zobach, Reservoir geomechanics, Cambridge Press2010.
[2] J.L. Yow, J.R. Hunt, Coupled processes in rock mass performance with emphasis on nuclear waste isolation, International Journal of Rock Mechanics and Mining Sciences, 39 (2002) 1-7.
[3] N.A. Rahman, R.W. Lewis, Finite element modelling of multiphase immiscible flow in deforming porous media for subsurface systems, Computers and Geotechnics, 24 (1999) 41-63.
[4] A.R. Khoei, T. Mohammadnejad, Numerical modeling of multiphase fluid flow in deforming porous media: A comparison between two- and three-phase models for seismic analysis of earth and rockfill dams, Computers and Geotechnics, 38 (2011) 142-166.
[5] M. Hassanizadeh, W.G. Gray, General conservation equations for multi-phase systems: 1. Averaging procedure, Advances in Water Resources, 2 (1979) 131-144.
[6] M. Hassanizadeh, W.G. Gray, General conservation equations for multi-phase systems: 2. Mass, momenta, energy, and entropy equations, Advances in Water Resources, 2 (1979) 191-203.
[7] X. Li, O.C. Zienkiewicz, Y.M. Xie, A numerical model for immiscible two-phase fluid flow in a porous medium and its time domain solution, International Journal for Numerical Methods in Engineering, 30 (1990) 1195-1212.
[8] L. Xikui, O.C. Zienkiewicz, Multiphase flow in deforming porous media and finite element solutions, Computers & Structures, 45 (1992) 211-227.

[9] B.A. Schrefler, Z. Xiaoyong, A fully coupled model for water flow and airflow in deformable porous media, Water Resources Research, 29 (1993) 155-167.
[10] A. Settari, F.M. Mourits, A Coupled Reservoir and Geomechanical Simulation System, SPE Journal, 3 (1998) 219-226.
[11] X. Li, H.R. Thomas, Y. Fan, Finite element method and constitutive modelling and computation for unsaturated soils, Computer Methods in Applied Mechanics and Engineering, 169 (1999) 135-159.
[12] L.K. Thomas, L.Y. Chin, R.G. Pierson, J.E. Sylte, Coupled geomechanics and reservoir simulation, SPE Journal, 8 (2003) 350-358.
[13] S.E. Minkoff, N.M. Kridler, A comparison of adaptive time stepping methods for coupled flow and deformation modeling, Applied Mathematical Modelling, 30 (2006) 993-1009.
[14] D. Sheng, A. Gens, D.G. Fredlund, S.W. Sloan, Unsaturated soils: From constitutive modelling to numerical algorithms, Computers and Geotechnics, 35 (2008) 810-824.
[15] J. Kim, H.A. Tchelepi, R. Juanes, Stability, Accuracy, and Efficiency of Sequential Methods for Coupled Flow and Geomechanics, SPE Journal, 16 (2011) 249-262.
[16] D. Yang, G.J. Moridis, T.A. Blasingame, A fully coupled multiphase flow and geomechanics solver for highly heterogeneous porous media, Journal of Computational and Applied Mathematics, 270 (2014) 417-432.
[17] S.A. Sadrnejad, H. Ghasemzadeh, E. Taheri, Multiscale multiphysic mixed geomechanical model in deformable porous media, International Journal for Multiscale Computational Engineering, 12 (2014) 529-547.
[18] J. Kim, W. Wang, R.A. Regueiro, Hybrid time integration and coupled solution methods for nonlinear finite element analysis of partially saturated deformable porous media at small strain, International Journal for Numerical and Analytical Methods in Geomechanics, 39 (2015) 1073-1103.
[19] R. Asadi, B. Ataie-Ashtiani, A comparison of finite volume formulations and coupling strategies for two-phase flow in deforming porous media, Computers and Geotechnics, 67 (2015) 17-32.
[20] L. Jeannin, M. Mainguy, R. Masson, S. Vidal-Gilbert, Accelerating the convergence of coupled geomechanical-reservoir simulations, International Journal for Numerical and Analytical Methods in Geomechanics, 31 (2007) 1163-1181.
[21] M. Gutierrez, R.W. Lewis, I. Masters, Petroleum Reservoir Simulation Coupling Fluid Flow and Geomechanics, SPE Reservoir Evaluation & Engineering, 4 (2001) 164-172.
[22] P.A. Beneyto, H.A. Di Rado, J.L. Mroginski, A.M. Awruch, A versatile mathematical approach for environmental geomechanic modelling based on stress state decomposition, Applied Mathematical Modelling, 39 (2015) 6880–6896.
[23] B. Jha, R. Juanes, A locally conservative finite element framework for the simulation of coupled flow and reservoir geomechanics, Acta Geotechnica, 2 (2007) 139-153.
[24] P. Phillips, M. Wheeler, A coupling of mixed and continuous Galerkin finite element methods for poroelasticity I: the continuous in time case, Computational Geosciences, 11 (2007) 131-144.
[25] M. Ferronato, N. Castelletto, G. Gambolati, A fully coupled 3-D mixed finite element model of Biot consolidation, Journal of Computational Physics, 229 (2010) 4813-4830.
[26] P.A. Forsyth, A Control-Volume, Finite-Element Method for Local Mesh Refinement in Thermal Reservoir Simulation, SPE Reservoir Engineering, 5 (1990) 561-566.
[27] L.S.K. Fung, A.D. Hiebert, L.X. Nghiem, Reservoir Simulation With a Control-Volume Finite-Element Method, SPE Reservoir Engineering, 7 (1992) 349-357.

[28] G. Gottardi, D. Dall'Olio, A control-volume finite-element model for simulating oil-water reservoirs, Journal of Petroleum Science and Engineering, 8 (1992) 29-41.
[29] S. Verma, Flexible grids for reservoir simulation, Department of Petroleum Engineering, Ph.D Dissertation, University of Stanford, 1996.
[30] Z. Chen, G. Huan, H. Wang, Simulation of a compositional model for multiphase flow in porous media, Numerical Methods for Partial Differential Equations, 21 (2005) 726-741.
[31] U.T. Mello, J.R.P. Rodrigues, A.L. Rossa, A control-volume finite-element method for three-dimensional multiphase basin modeling, Marine and Petroleum Geology, 26 (2009) 504-518.
[32] S.A. Sadrnejad, H. Ghasemzadeh, S.A. Ghoreishian Amiri, G.H. Montazeri, A control volume based finite element method for simulating incompressible two-phase flow in heterogeneous porous media and its application to reservoir engineering, Petroleum Science, 9 (2012) 485-497.
[33] S.A. Ghoreishian Amiri, S.A. Sadrnejad, H. Ghasemzadeh, G.H. Montazeri, Application of control volume based finite element method for solving the black-oil fluid equations, Petroleum Science, 10 (2013) 361-372.
[34] L.J. Durlofsky, Accuracy of mixed and control volume finite element approximations to Darcy velocity and related quantities, Water Resources Research, 30 (1994) 965-973.
[35] C.A. Lujan, Three-phase flow analysis of soil spills in partially water-saturated soil, Department of Civil Engineering, Ph.D Dissertation, Colorado State University, 1985.
[36] S.M. Hassanizadeh, W.G. Gray, Thermodynamic basis of capillary pressure in porous media, Water Resources Research, 29 (1993) 3389-3405.
[37] R. Brooks, A. Corey, Properties of porous media affecting fluid flow, Journal of the Irrigation and Drainage Division, 92 (1966) 61-88.
[38] C.F. Wei, Static and dynamic behavior of multiphase porous media: Governing equations and finite element implementation, Ph.D Dissertation, University of Oklahoma, 2001.
[39] U. Nowak, L. Weimann, GIANT: A software package for the numerical solution of very large systems of highly nonlinear equations, Konrra-Zuse-Zentrum fuer Informationstechnik Berlin, 1990.
[40] A. Settari, K. Aziz, Treatment of nonlinear terms in the numerical solution of partial differential equations for multiphase flow in porous media, International Journal of Multiphase Flow, 1 (1975) 817-844.
[41] M.B. Reed, An investigation of numerical errors in the analysis of consolidation by finite elements, International Journal for Numerical and Analytical Methods in Geomechanics, 8 (1984) 243-257.
[42] R.W. Lewis, B.A. Schrefler, The finite element method in the deformation and consolidation of porous media, 1987.
[43] S.W. Sloan, A.J. Abbo, Biot consolidation analysis with automatic time stepping and error control Part 1: theory and implementation, International Journal for Numerical and Analytical Methods in Geomechanics, 23 (1999) 467-492.
[44] C.J. van Duijn, M.J. de Neef, Similarity solution for capillary redistribution of two phases in a porous medium with a single discontinuity, Advances in Water Resources, 21 (1998) 451-461.
[45] H. Hoteit, A. Firoozabadi, Numerical modeling of two-phase flow in heterogeneous permeable media with different capillarity pressures, Advances in Water Resources, 31 (2008) 56-73.
[46] M.B. Das, Advanced soil mechanics, Third ed., Taylor & Francis2008.
[47] P.A. Vermeer, A. Verruijt, An accuracy condition for consolidation by finite elements, International Journal for Numerical and Analytical Methods in Geomechanics, 5 (1981) 1-14.

[48] J. Wan, Stabilized finite element methods for coupled geomechanics and multiphase flow, Ph.D Dissertation, stanford university, 2002.
[49] O. Bajor, D.E. Cormack, A New Method for Characterizing the Grid Orientation Phenomenon, Society of Petroleum Engineers.
[50] F.S.V. Hurtado, C.R. Maliska, A.F.C. Silva, On the factors influencing the grid orientation effect in reservoir simulation, 19th International Congress of Mechanical Engineering, Brasilia, 2007.
[51] J.L. Yanosik, T.A. McCracken, A Nine-Point, Finite-Difference Reservoir Simulator for Realistic Prediction of Adverse Mobility Ratio Displacements, (1979).
[52] B. Riviere, P. Bastian, Discontinuous Galerkin methods for two-phase flow in porous media, Klumer Academic Publisher: Netherlands, 2004.

Table 1. Material properties and model parameters for Van Duijn-De Neef Problem

	Case 1	Case 2
Rock porosity	$n = 0.25$	$n = 0.25$
Absolute permeability, darcy	$\begin{cases}(K)_{\text{part 1}} = 85.8 \\ (K)_{\text{part 2}} = 85.8\end{cases}$	$\begin{cases}(K)_{\text{part 1}} = 85.8 \\ (K)_{\text{part 2}} = 42.9\end{cases}$
Fluids viscosity, cP	$\mu_w = \mu_n = 1.$	$\mu_w = \mu_n = 1.$
Fluids density, ton/m^3	$\rho_w = \rho_n = 1.$	$\rho_w = \rho_n = 1.$
Relative permeability fitting parameter	$\lambda = 2.$	$\lambda = 2.$
Displacement pressure for non-wetting phase, kPa	$\begin{cases}(p_d)_{\text{part 1}} = 10. \\ (p_d)_{\text{part 2}} = 10.\end{cases}$	$\begin{cases}(p_d)_{\text{part 1}} = 10. \\ (p_d)_{\text{part 2}} = 14.1\end{cases}$
Wetting phase residual volume fraction	$n_{wres} = 0.001$	$n_{wres} = 0.001$

Table 2. Material properties and model parameters for radial flow problem

Elastic modulus, kPa	$E = 1.E7$
Poisson's Ratio	$\upsilon = 0.3$
Rock porosity	$n = 0.208$
Rock permeability, mD	$k = 15.$
Oil viscosity, cP	$\mu_o = 1.$
Water viscosity, cP	$\mu_w = 0.01$
Oil density, ton/m^3	$\rho_0 = 0.85$
Water density, ton/m^3	$\rho_w = 1.$
Relative permeability fitting parameter	$\lambda = 0.8$
Displacement pressure for non-wetting phase, kPa	$p_d = 2.$
Water residual volume fraction	$n_{wres} = 0.045$

Table 3. Material properties and model parameters for continuous heterogeneous problem

Elastic modulus, kPa	$E = 1.E7$
Poisson's Ratio	$\upsilon = 0.3$
Rock porosity	$n = 0.208$
Oil viscosity, cP	$\mu_o = 13.$
Water viscosity, cP	$\mu_w = 0.97$
Oil density, ton/m^3	$\rho_0 = 0.75$
Water density, ton/m^3	$\rho_w = 1.$
Oil compressibility, vol/vol kPa	$C_o = 4.E-8$
Water compressibility, vol/vol kPa	$C_w = 4.E-9$
Relative permeability fitting parameter	$\lambda = 0.8$
Displacement pressure for non-wetting phase, kPa	$p_d = 2.$
Water residual volume fraction	$n_{wres} = 0.045$

Table 4. Computational information for continuous heterogeneous problem

No. Elements	No. nodes	No. Time steps	CPU time (min)
1424	2304	31	108

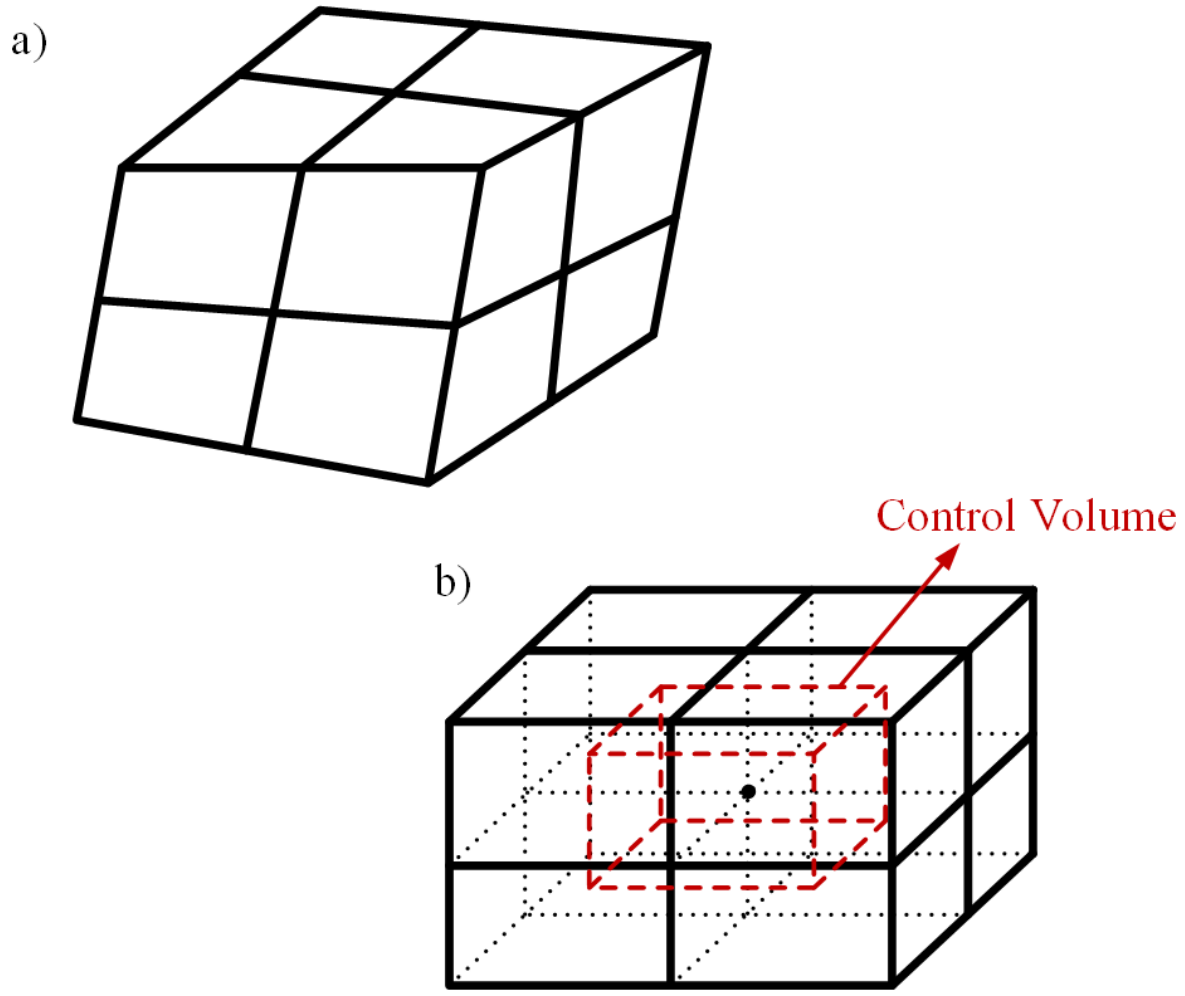

Fig. 1. a) System of finite the element mesh in the physical space; and b) representation of a control volume around a node in the transformed space

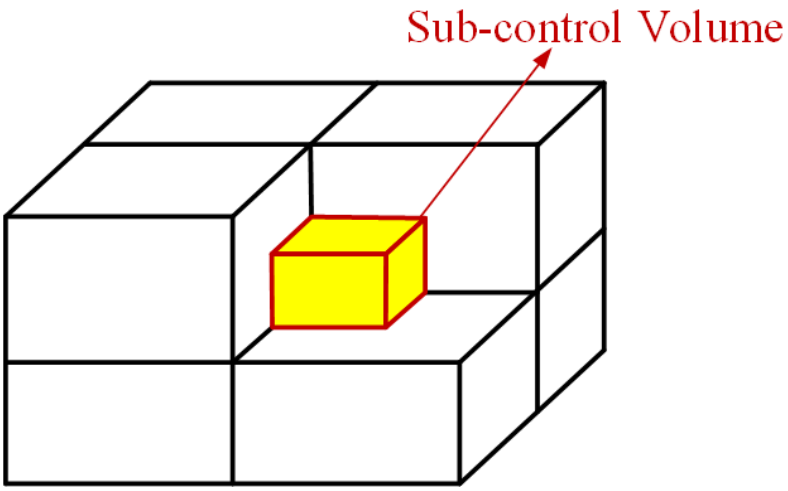

Fig. 2. Sub-control volume representation

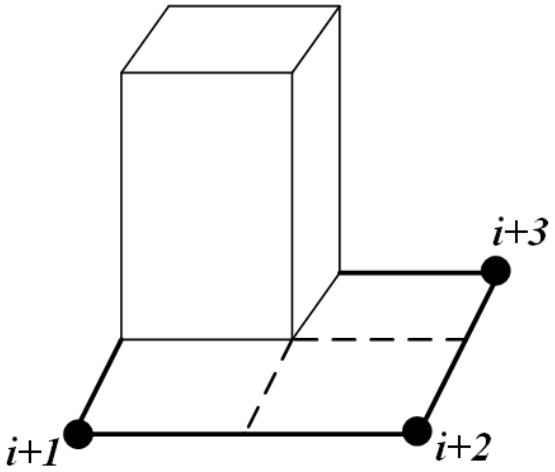

Fig. 3. The control volume finite element weighting function for node *i* (two dimensional case)

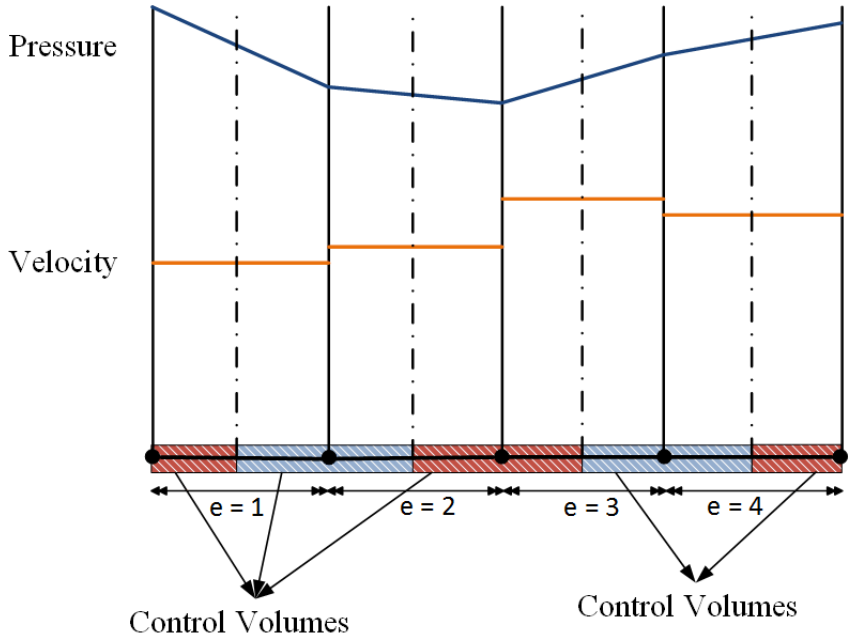

Fig. 4. Schematic of pressure and velocity distribution for a one dimensional finite element mesh

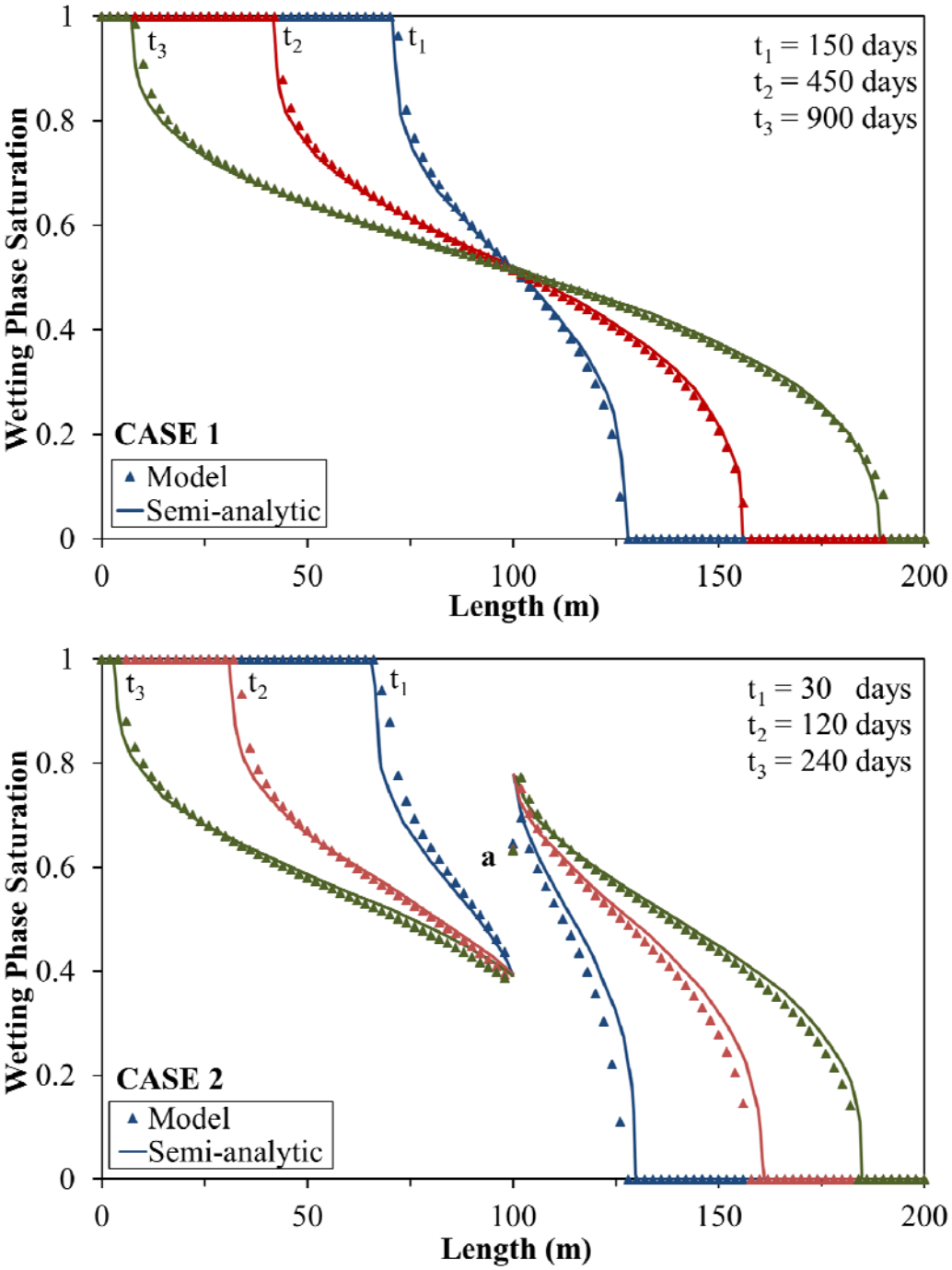

Fig. 5. Numerical and semi-analytical results for Van Duijn-De Neef problem

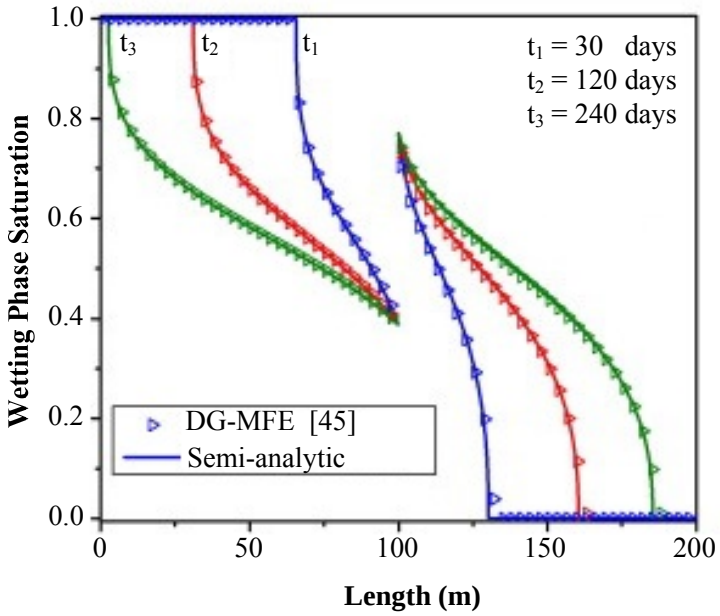

Fig. 6. Numerical and semi-analytical results for case 2 of Van Duijn-De Neef problem using mixed finite element-discontinuous Galerkin scheme (after [45])

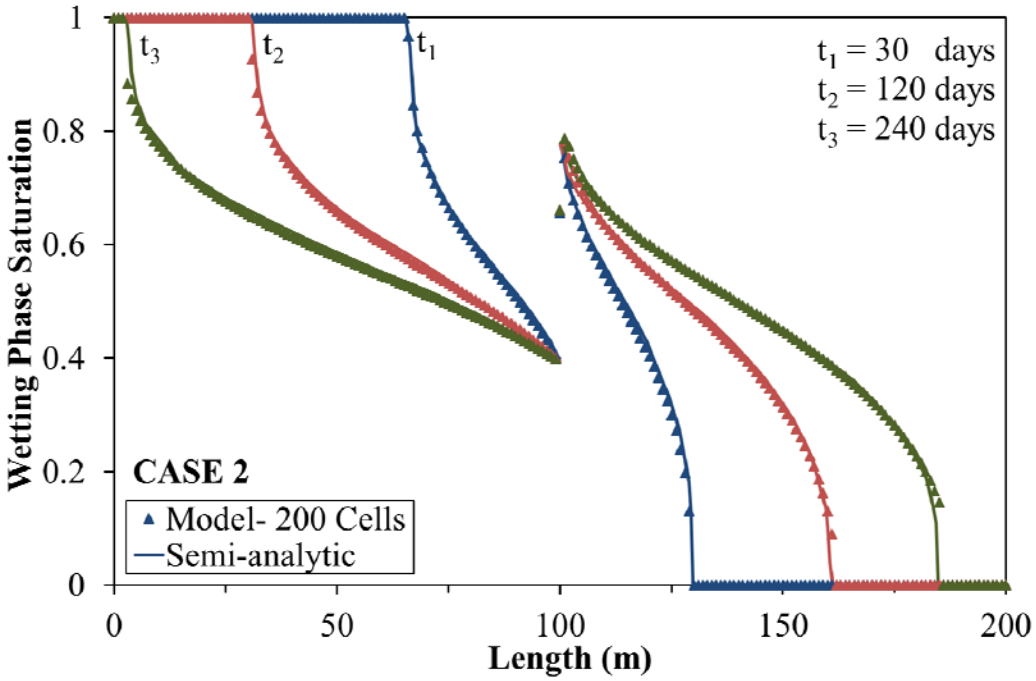

Fig. 7. Numerical and semi-analytical results for case 2 of Van Duijn-De Neef using 200 computational cells

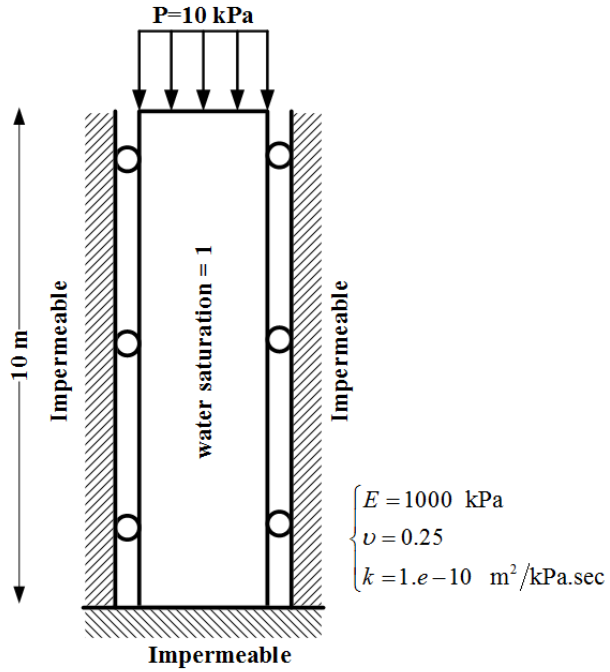

Figure 8. One dimensional-one phase consolidation problem

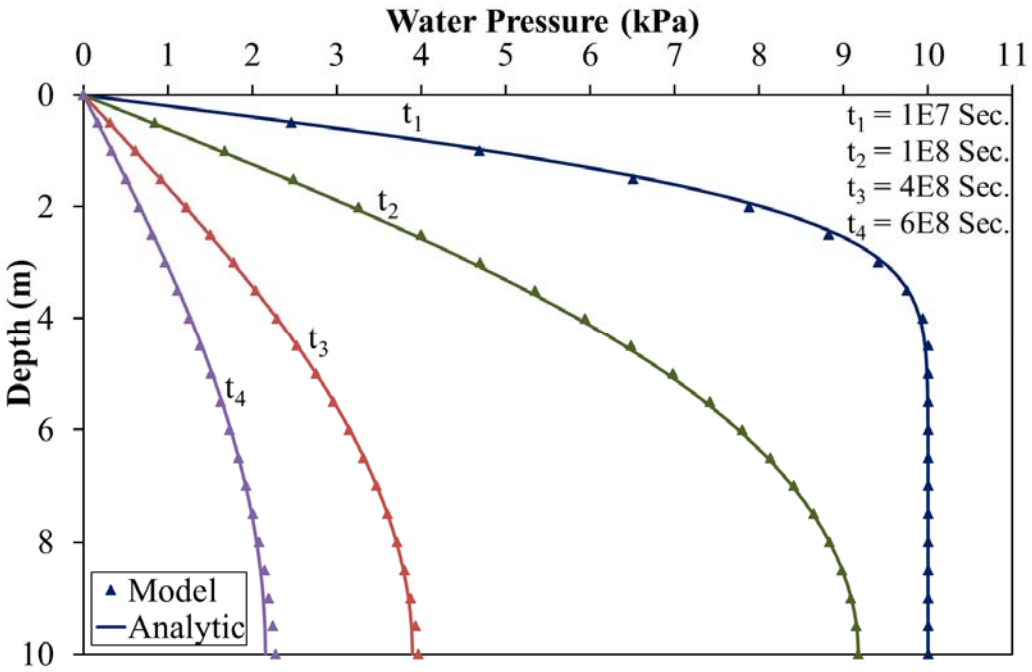

Figure 9. Numerical and analytical results for one dimensional-one phase consolidation problem

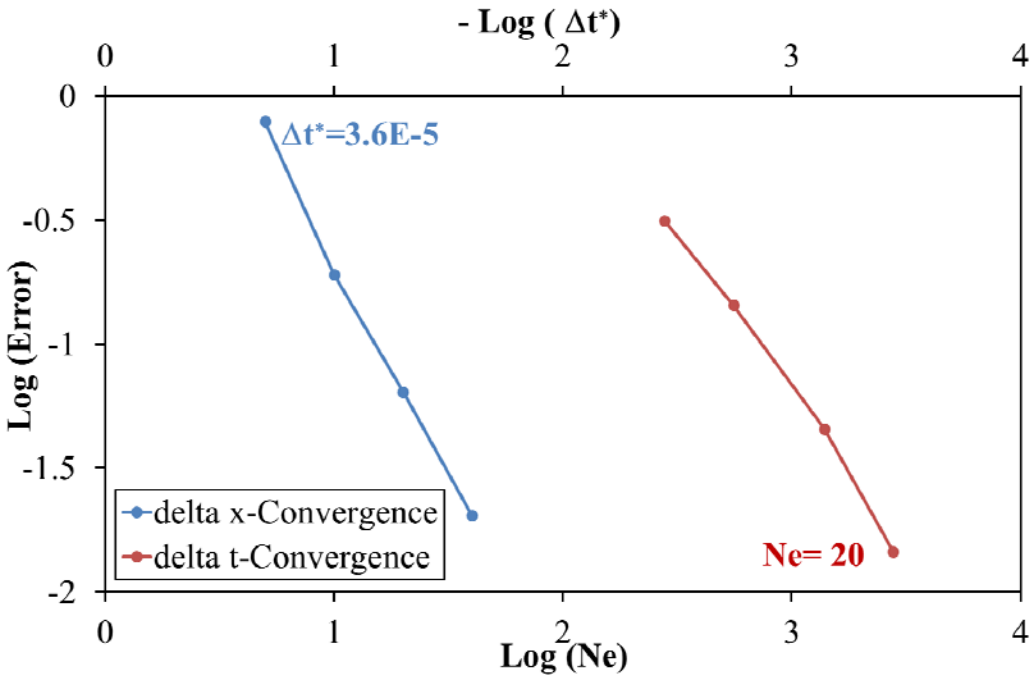

Figure 10. Convergence study for one dimensional-one phase consolidation problem

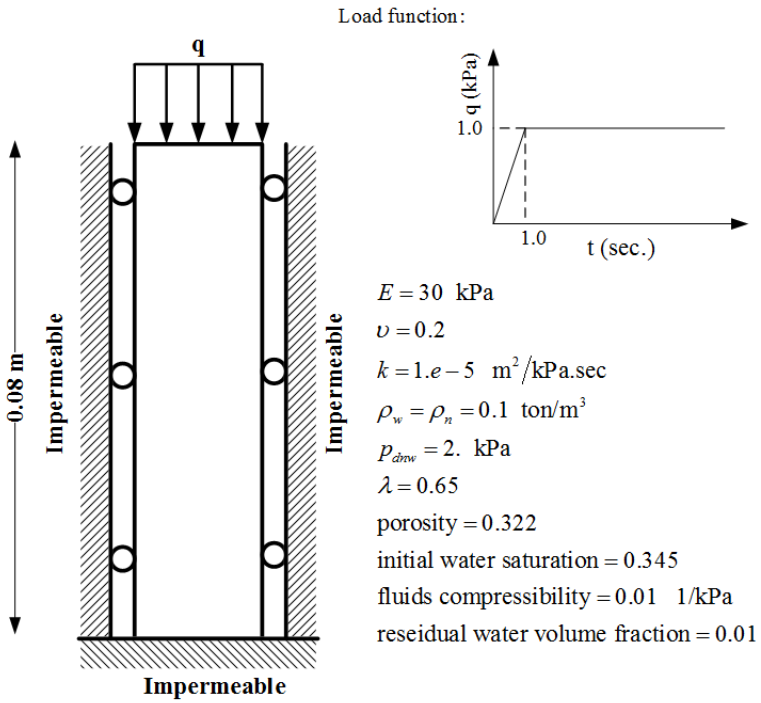

Figure 11. One dimensional-two phase consolidation problem

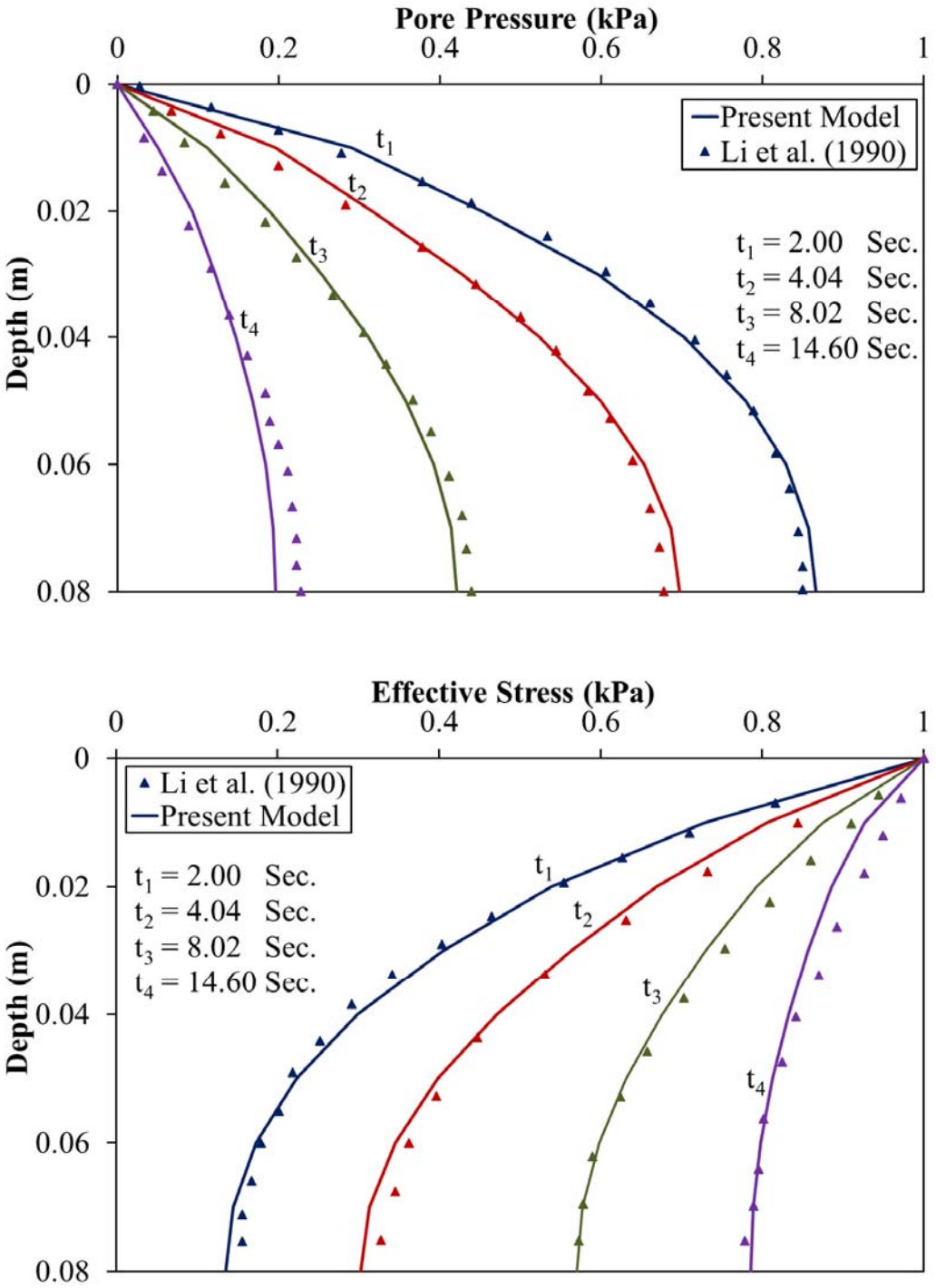

Figure 12. Numerical and analytical results for one dimensional-two phase consolidation problem

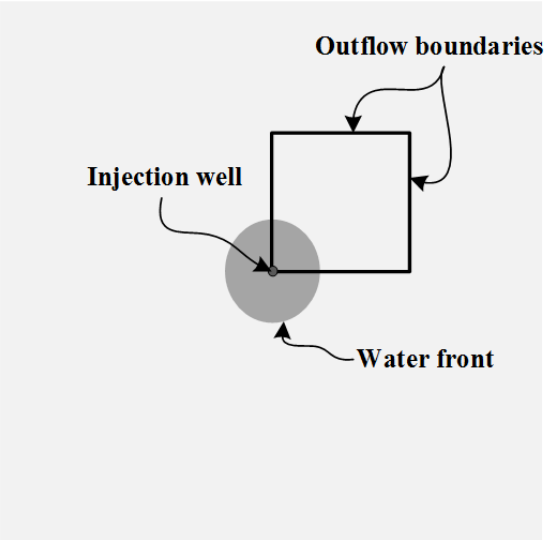

Figure 13. The radial flow problem (after [50])

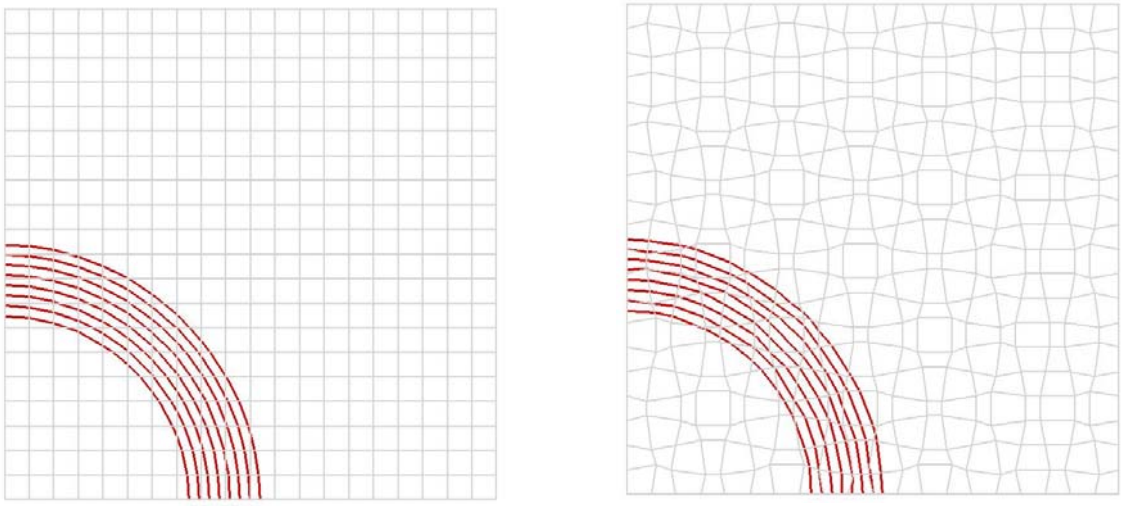

Figure 14. Water saturation contours after 0.2 PV of water injection for the radial flow problem on regular and randomly distorted grids (case 1)

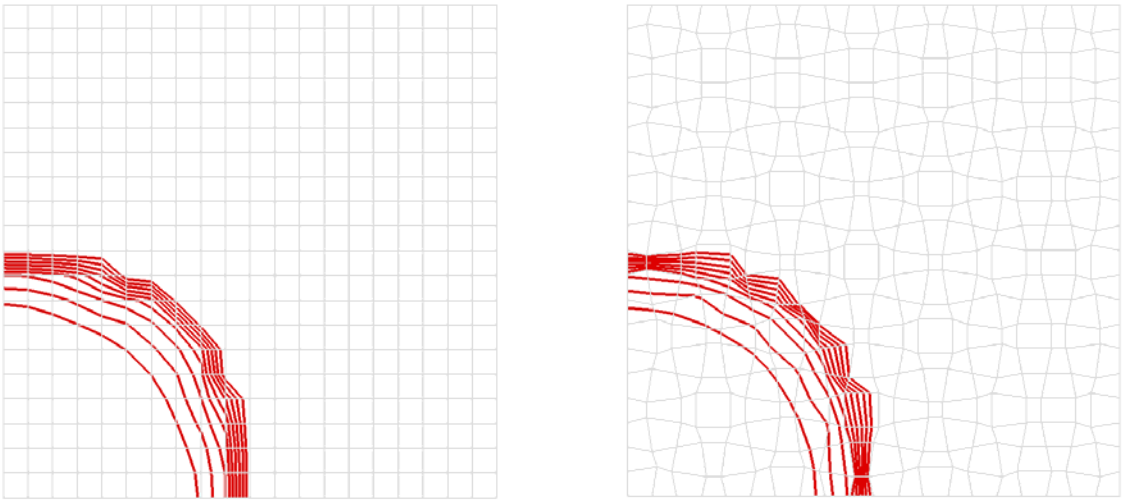

Figure 15. Water saturation contours after 0.2 PV of water injection for the radial flow problem on regular and randomly distorted grids (case 2)

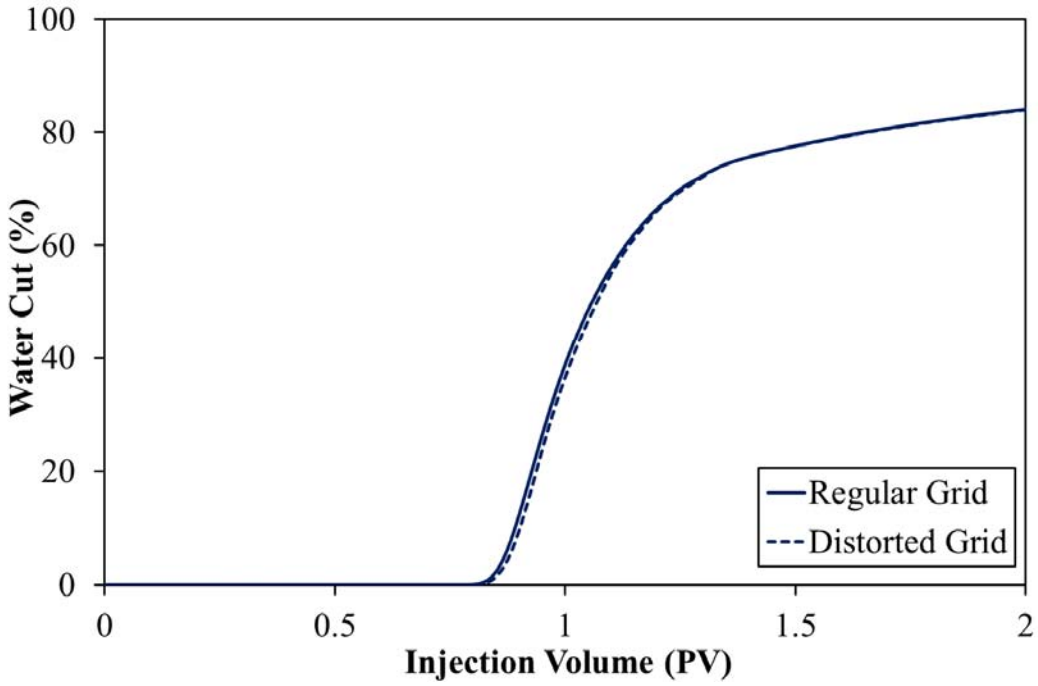

Figure 16. Water cut curves for the radial flow problem (case 2)

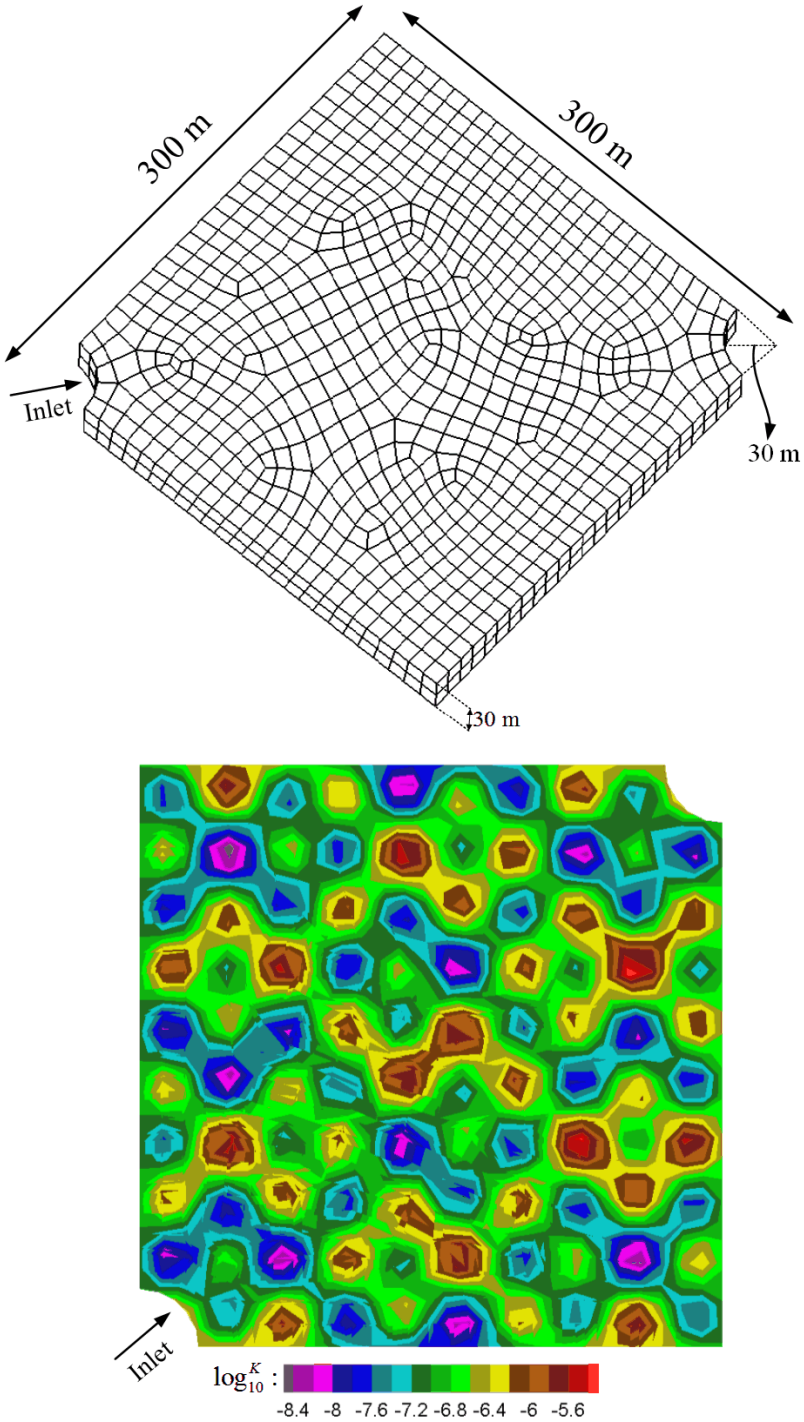

Figure 17. Physical domain, finite element mesh and absolute permeability distribution for the continuous heterogeneous problem

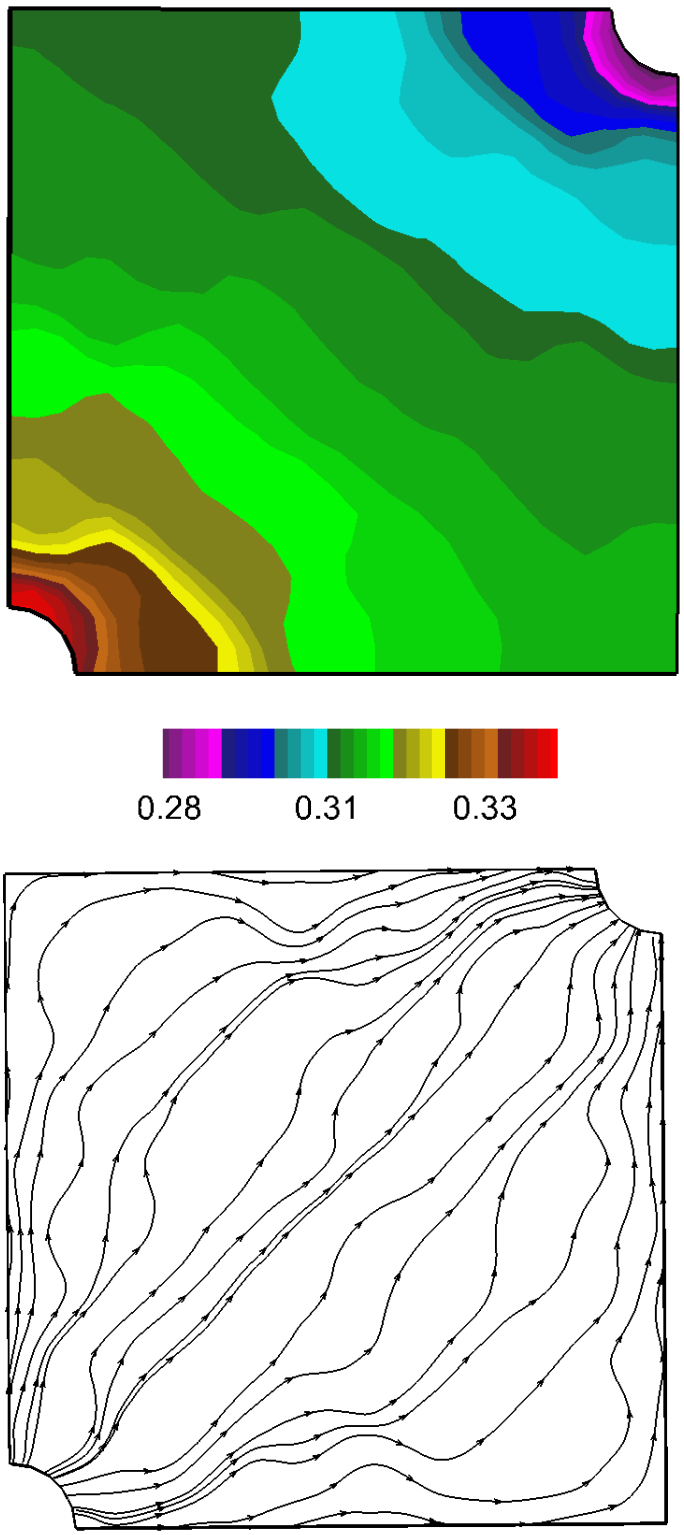

Figure 18. Water saturation distribution and streamlines for the continuous heterogeneous problem

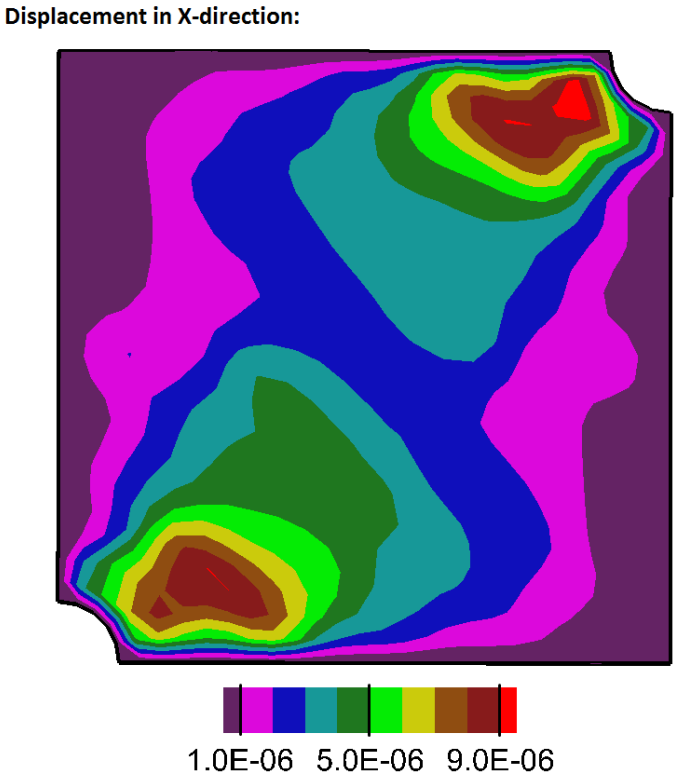

Figure 19. Displacement contours for the continuous heterogeneous problem